Available online at www.sciencedirect.com
SCIENCE DIRECT®
Journal of Sound and Vibration 276 (2004) 997–1017
JOURNAL OF SOUND AND VIBRATION
www.elsevier.com/locate/jsvi

# Free vibration and buckling analyses of shear-deformable plates based on FSDT meshfree method

K.M. Liew[a,b,*], J. Wang[a], T.Y. Ng[a,b], M.J. Tan[b]

[a] *Nanyang Centre for Supercomputing and Visualisation, Nanyang Technological University, Nanyang Avenue, Singapore 639798, Singapore*

[b] *School of Mechanical and Production Engineering, Nanyang Technological University, Nanyang Avenue, Singapore 639798, Singapore*

Received 3 March 2003; accepted 13 August 2003

**Abstract**

A meshfree method based on the reproducing kernel particle approximate is employed for the free vibration and buckling analyses of shear-deformable plates. In this approach, the first order Mindlin/Reissner plate theory (FSDT) is used, and the displacement shape functions are constructed using the reproducing kernel approximation satisfying the consistency condition. The essential boundary conditions are enforced by a transformation method. Numerical examples considering various aspect ratios, skew angles and boundary conditions are demonstrated to show the validity of the proposed method, and satisfactory results were obtained when comparisons are made with the exact and other available numerical results existing in the literature.


## 1. Introduction

The analysis of the free vibration of plates started at the early 1800s via studying the free vibration of a square plate with free edges. Subsequently, Rayleigh [1] introduced his general solution method to obtain the natural frequencies of vibration of structures. Later in 1909, Ritz developed Rayleigh's method by assuming a series of admissible trial functions with independent amplitude coefficients. After this came the well-known Rayleigh–Ritz method, which is one of the most commonly used approximate methods for the vibration analysis of structures. Since then,

*Corresponding author. School of Mechanical and Production Engineering, Nanyang Technological University, Nanyang Avenue, Singapore 639798, Singapore. Tel.: +65-6790-4076; fax: +65-6793-6763.
*E-mail address:* mkmliew@ntu.edu.sg (K.M. Liew).

0022-460X/$ - see front matter 
doi:10.1016/j.jsv.2003.08.026

many investigations have been undertaken into the vibration analysis of plates with various shapes, boundary conditions and loadings. In the early period, most of the reports concentrated on thin plates, for which the transverse shear influences were not considered. The classical plate theories based on the Kirchhoff hypothesis, are often used for thin plates. However, these classical theories are inadequate to predict the gross response characteristics of moderately thick laminated composite plates as well as plates with high anisotropy. Usually in thicker plates, the vibration solutions are unconservatively high. The inaccuracy is caused by ignoring the transverse shear and normal strains in the plates. Thus, many shear-deformation plate theories were developed to improve the analysis of the vibration of plates, and this has led to more accurate results. Among the theories, the Mindlin-type first order shear-deformation plate theory (FSDT) was most commonly used. The FSDT assumes constant transverse shear strains along the thickness direction, and requires shear correction factors to modify the transverse shear stiffness for the analysis of plates. Usually, FSDT is sufficient and quite accurate for the natural frequencies of moderately thick plates.

There are several excellent review papers concerning the vibration analysis of plates using various plate theories, including higher order deformation plate theories and the three-dimensional elasticity theory. One can find more detailed information about the studies of plate vibrations from these review papers, viz. Liew et al. [2], Noor [3], Reddy [4] and Tessler et al. [5].

The buckling analysis of plates is another class of eigenvalue problem. As is well known, a plate may lose its ability to withstand the external loadings, when the in-plane strain reaches a critical level. This phenomenon is the buckling of the plate, and the corresponding critical load at which the plate starts to become unstable, is termed the buckling load.

To analyze the buckling behavior of a thin plate, the classical plate theory (CPT) is often used. However, similar to the vibration of plates, when the thickness of the plate increases, the transverse shear-deformation effects will significantly influence the results of the buckling analysis. Thus the CPT is not applicable, and shear deformable plate theories are often resorted to. Furthermore, the use of CPT may result in a different buckling mode shape compared with those of other plate theories, such as 3D elasticity theory, FSDT or higher order shear-deformation theory (HSDT).

Many methodologies have been implemented for various plate buckling and free vibration problems. These methods include analytical and numerical techniques, such as the Ritz method [6–16], differential quadrature method [17,18], finite strip methods [19] and the finite element method [20,21], etc. Some reviews of the literature on buckling analysis of laminated composite plates may be found from Leissa [22,23] and Kapania et al. [24].

In this paper, a meshfree method based on the reproducing kernel particle approximation is employed for the buckling and free vibration analyses of shear-deformable plates. The first order Mindlin/Reissner shear-deformation theory is adopted to incorporate the shear-deformation effects. For numerical implementation, the essential boundary conditions are enforced by a transformation so as to ease the treatment of the boundaries in the source code programming. Numerical results obtained for the free vibration analysis of rectangular and circular plates with various thickness ratios and boundary conditions, and buckling analysis of rectangular and skew plates subjected to different boundary conditions show that the present method is effective and accurate for the free vibration and buckling analysis of shear-deformable plates.

## 2. Formulations for free vibration and buckling

### 2.1. Variational formulation of Mindlin plates

A typical Mindlin/Reissner plate with notations shown in Fig. 1 is considered here. For an initially flat isotropic thick plate, the membrane deformations are not accounted for since they are uncoupled from the bending and shear deformations. Hence, the basic assumptions for displacement behavior [20,25] are

$$\mathbf{u}(x,y,z)=\begin{Bmatrix} u(x,y,z)\\ v(x,y,z)\\ w(x,y,z)\end{Bmatrix}=\begin{Bmatrix} z\theta_x(x,y)\\ z\theta_y(x,y)\\ w(x,y)\end{Bmatrix}, \tag{1}$$

where $u(x,y,z)$, $v(x,y,z)$ and $w(x,y,z)$ are the components of displacement at a general point, whilst $w(x,y)$ is the transverse deflection at the middle surface. The quantities $\theta_x(x,y)$ and $\theta_y(x,y)$ are the rotations in the $x$ and $y$ directions, respectively. Incorporating the fundamental Mindlin/Reissner plate theory, the bending and shear strains are taken as

$$\boldsymbol{\varepsilon}_b=\begin{bmatrix}\theta_{x,x}\\ \theta_{y,y}\\ \theta_{x,y}+\theta_{y,x}\end{bmatrix},\quad \boldsymbol{\varepsilon}_s=\begin{bmatrix}\theta_x+w_{,x}\\ \theta_y+w_{,y}\end{bmatrix}. \tag{2}$$

The free vibration analysis of a Mindlin/Reissner plate may start from the dynamic version of energy principle of virtual displacement incorporating the first order shear-deformation plate theory:

$$\iint \delta\boldsymbol{\varepsilon}_b^{\mathrm{T}}\mathbf{D}_b\boldsymbol{\varepsilon}_b\,\mathrm{d}x\,\mathrm{d}y+\iint \delta\boldsymbol{\varepsilon}_s^{\mathrm{T}}\mathbf{D}_b\boldsymbol{\varepsilon}_s\,\mathrm{d}x\,\mathrm{d}y+\iint \delta\mathbf{u}^{\mathrm{T}}\mathbf{B}_m\ddot{\mathbf{u}}\,\mathrm{d}x\,\mathrm{d}y=0. \tag{3}$$

For the buckling analysis, when the plate is subjected to in-plane pre-buckling stresses $\sigma_x^0,\sigma_y^0,\tau_{xy}^0$, and in the absence of external forces, the potential energy is written as

$$\begin{aligned}\Pi=&\frac{1}{2}\iint \boldsymbol{\varepsilon}_b^{\mathrm{T}}\mathbf{D}_b\boldsymbol{\varepsilon}_b\,\mathrm{d}x\,\mathrm{d}y+\frac{1}{2}\iint \boldsymbol{\varepsilon}_s^{\mathrm{T}}\mathbf{D}_s\boldsymbol{\varepsilon}_s\,\mathrm{d}x\,\mathrm{d}y+\frac{1}{2}\iint [w_{,x}\quad w_{,y}]\hat{\boldsymbol{\sigma}}_0\begin{Bmatrix}w_{,x}\\ w_{,y}\end{Bmatrix}t\,\mathrm{d}x\,\mathrm{d}y\\ &+\frac{1}{2}\iint [\theta_{x,x}\quad \theta_{x,y}]\hat{\boldsymbol{\sigma}}_0\begin{Bmatrix}\theta_{x,x}\\ \theta_{x,y}\end{Bmatrix}\frac{t^3}{12}\mathrm{d}x\,\mathrm{d}y+\frac{1}{2}\iint [\theta_{y,x}\quad \theta_{y,y}]\hat{\boldsymbol{\sigma}}_0\begin{Bmatrix}\theta_{y,x}\\ \theta_{y,y}\end{Bmatrix}\frac{t^3}{12}\mathrm{d}x\,\mathrm{d}y.\end{aligned} \tag{4}$$

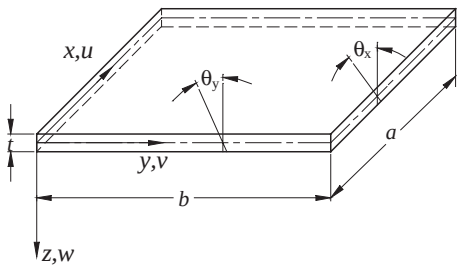


Fig. 1. Geometry notation of a typical Mindlin/Reissner plate.

In Eqs. (3) and (4), the coefficient matrices are defined as

$$\hat{\boldsymbol{\sigma}}_0 = \begin{bmatrix} \sigma_x^0 & \tau_{xy}^0 \\ \tau_{xy}^0 & \sigma_y^0 \end{bmatrix}, \quad \mathbf{D}_b = \frac{Et^3}{12(1-v^2)} \begin{bmatrix} 1 & v & 0 \\ v & 1 & 0 \\ 0 & 0 & (1-v)/2 \end{bmatrix}, \tag{5a}$$

$$\mathbf{D}_s = \frac{\kappa^2 Et}{2(1+v)} \begin{bmatrix} 1 & 0 \\ 0 & 1 \end{bmatrix}, \quad \mathbf{B}_m = \rho \begin{bmatrix} t & 0 & 0 \\ & t^3/12 & 0 \\ sym. & & t^3/12 \end{bmatrix}, \tag{5b}$$

where $E$ is Young's modulus, $v$ the Poisson ratio, $\rho$ the plate density, and $\kappa^2$ the transverse shear correction factor.

### 2.2. Reproducing kernel approximation form

In the reproducing kernel equation, a function $u(\mathbf{x})$ in the domain $\Omega_x$, is reproduced through the following kernel transformation [26]:

$$u^a(\mathbf{x}) = \int_{\Omega_x} \kappa(\mathbf{x}; \mathbf{x}-\mathbf{y}) u(\mathbf{y})\, \mathrm{d}\mathbf{y}, \tag{6}$$

in which, $u^a(\mathbf{x})$ is the reproduced function and $\kappa(\mathbf{x}; \mathbf{x}-\mathbf{y})$ is the reproducing kernel function defined as

$$\kappa(\mathbf{x}; \mathbf{x}-\mathbf{y}) = \boldsymbol{\Phi}_a(\mathbf{x}-\mathbf{y}) C(\mathbf{x}; \mathbf{x}-\mathbf{y}), \tag{7}$$

where $\boldsymbol{\Phi}_a(\mathbf{x}; \mathbf{x}-\mathbf{y})$ is the kernel function or window function with compact support and $C(\mathbf{x}; \mathbf{x}-\mathbf{y})$ is the correction function solved by satisfying reproducing conditions. The reproducing conditions require the approximated functions and their derivatives to be exactly reproduced over the entire domain.

To solve a partial differential problem, one can discretize the domain $\Omega_x$ into $NP$ scattered particles/nodes $(\mathbf{x}_1, \mathbf{x}_2, \ldots, \mathbf{x}_{NP})$, then write the kernel approximate as

$$u^a(\mathbf{x}) \cong \sum_{I=1}^{NP} \kappa(\mathbf{x}; \mathbf{x}-\mathbf{x}_I) u(\mathbf{x}_I) \Delta \mathbf{V}_I \equiv \sum_{I=1}^{NP} \mathbf{N}_I^a(\mathbf{x}) \mathbf{u}_I, \tag{8}$$

in which, $\Delta \mathbf{V}_I$ is the volume associated with the particle $\mathbf{x}_I$ and can be simply set to unity, and $\mathbf{N}_I^a(\mathbf{x})$ and $u(\mathbf{x}_I)$ are the shape function and the corresponding nodal parameters of the reproducing kernel approximation, respectively.

Using the methodology laid out in the preceding section on the variational form of Eqs. (3) and (4), the following expansions in terms of the approximation shape functions, $\mathbf{N}_I^a$, and its derivatives can be written as

$$\boldsymbol{\delta} = \sum_{I=1}^{NP} \mathbf{N}_I \mathbf{d}_I, \quad \boldsymbol{\varepsilon}_b = \sum_{I=1}^{NP} \mathbf{B}_{bI} \mathbf{d}_I, \quad \boldsymbol{\varepsilon}_s = \sum_{I=1}^{NP} \mathbf{B}_{sI} \mathbf{d}_I,$$

$$\begin{Bmatrix} w_{,x} \\ w_{,y} \end{Bmatrix} = \sum_{I=1}^{NP} \mathbf{G}_{bI} \mathbf{d}_I, \quad \begin{Bmatrix} \theta_{x,x} \\ \theta_{x,y} \end{Bmatrix} = \sum_{I=1}^{NP} \mathbf{G}_{s1I} \mathbf{d}_I, \quad \begin{Bmatrix} \theta_{y,x} \\ \theta_{y,y} \end{Bmatrix} = \sum_{I=1}^{NP} \mathbf{G}_{s2I} \mathbf{d}_I, \tag{9}$$

where

$$\boldsymbol{\delta} = [w \quad \theta_x \quad \theta_y]^{\mathrm{T}}, \quad \mathbf{d}_I = [w_I \quad \theta_{xI} \quad \theta_{yI}]^{\mathrm{T}} \tag{10}$$

and

$$\mathbf{N}_I = \begin{bmatrix} N_I^a & 0 & 0 \\ 0 & N_I^a & 0 \\ 0 & 0 & N_I^a \end{bmatrix}, \quad \mathbf{B}_{bI} = \begin{bmatrix} 0 & N_{I,x}^a & 0 \\ 0 & 0 & N_{I,y}^a \\ 0 & N_{I,y}^a & N_{I,x}^a \end{bmatrix}, \tag{11a}$$

$$\mathbf{B}_{sI} = \begin{bmatrix} N_{I,x}^a & N_I^a & 0 \\ N_{I,y}^a & 0 & N_I^a \end{bmatrix}, \quad \mathbf{G}_{bI} = \begin{bmatrix} N_{I,x}^a & 0 & 0 \\ N_{I,y}^a & 0 & 0 \end{bmatrix}, \tag{11b}$$

$$\mathbf{G}_{s1I} = \begin{bmatrix} 0 & N_{I,x}^a & 0 \\ 0 & N_{I,y}^a 0 & 0 \end{bmatrix}, \quad \mathbf{G}_{s2I} = \begin{bmatrix} 0 & 0 & N_{I,x}^a \\ 0 & 0 & N_{I,y}^a \end{bmatrix}. \tag{11c}$$

Hence, the RKPM formulation for free vibration of a Mindlin/Reissner plate can be written in matrix form as

$$(\mathbf{K} - \omega_I^2 \underline{\mathbf{M}})\mathbf{d}_I = 0, \quad I = 1, 2, \ldots, N_f, \tag{12}$$

where $\mathbf{K}$ is the global stiffness matrix, $\underline{\mathbf{M}}$ is the global mass matrix, the column vector $\mathbf{d}_I$ contains the vibration mode shapes, $N_f$ is the total number of vibration modes, which is also the total number of the degrees of freedom, and $\omega_I$ is the $I$th natural frequency. And the buckling equation is obtained as

$$(\mathbf{K} - \lambda \mathbf{K}_G)\mathbf{d} = 0, \tag{13}$$

in which $\mathbf{K}$ is the same as in Eq. (12), and $\mathbf{K}_G$ is the geometrical stiffness matrix, and $\lambda$ is a scalar by which the chosen in-plane loads must be multiplied by in order to cause buckling. By substituting Eq. (9) into Eqs. (3)–(4) and differentiating the principle potential energy, the stiffness matrices can be obtained as

$$\mathbf{K} = \int_\Omega \mathbf{B}_b^{\mathrm{T}} \mathbf{D}_b \mathbf{B}_b \, \mathrm{d}\Omega + \int_\Omega \mathbf{B}_s^{\mathrm{T}} \mathbf{D}_s \mathbf{B}_s \, \mathrm{d}\Omega, \tag{14a}$$

$$\mathbf{K}_G = t \int_\Omega \mathbf{G}_b^{\mathrm{T}} \hat{\boldsymbol{\sigma}}_0 \mathbf{G}_b \, \mathrm{d}\Omega + \frac{t^3}{12} \int_\Omega \mathbf{G}_{s1}^{\mathrm{T}} \hat{\boldsymbol{\sigma}}_0 \mathbf{G}_{s1} \, \mathrm{d}\Omega + \frac{t^3}{12} \int_\Omega \mathbf{G}_{s2}^{\mathrm{T}} \hat{\boldsymbol{\sigma}}_0 \mathbf{G}_{s2} \, \mathrm{d}\Omega. \tag{14b}$$

In the RKPM approximation, the shape functions describing the variation of the acceleration field over the domain of influence of each particle are the same as those for the displacement variation. The related mass matrix is known as the so-called consistent mass matrix as in FEM implementation. This type of mass matrix takes into consideration the effects of rotary inertia.

The mass matrix in RKPM implementation is computed as

$$\underline{\mathbf{M}}_{IJ} = \left( \int_{\Omega} N_I^{\mathrm{T}} N_J \, \mathrm{d}\Omega \right) \mathbf{B}_m. \tag{15}$$

### 2.3. Enforcement of essential boundary conditions via transformation

Due to the lack of Kronecker delta properties in the reproducing kernel particle approximate, the essential boundary conditions can be attained but not without additional complications. Many methods, such as the Lagrange multiplier method, penalty method, boundary singular kernel method [26,27], etc., have been developed for the enforcement of essential boundary conditions. Here the transformation method, which was proposed by Chen et al. [26], is employed to impose the essential boundary conditions. This method was chosen because of its ease of coding, however, it may lead to a change in the sparse property of the stiffness matrices and result in higher computation expense. In this implementation, the stiffnesses $\mathbf{K}$, $\mathbf{K}_G$, the mass matrix $\underline{\mathbf{M}}$, and the nodal parameter $\mathbf{d}$ are transformed by using a transformation matrix, then the final free vibration and buckling equations are obtained as

$$(\hat{\mathbf{K}} - \hat{\omega}_I^2 \hat{\underline{\mathbf{M}}}) \hat{\mathbf{d}}_I = 0, \tag{16a}$$

$$(\hat{\mathbf{K}} - \lambda \hat{\mathbf{K}}_G) \hat{\mathbf{d}} = 0. \tag{16b}$$

Consequently, the essential boundary conditions are imposed simply by following FEM methodology [20]. The transformed matrices are given as

$$\hat{\mathbf{K}} = \mathbf{\Lambda}^{-1} \mathbf{K} \mathbf{\Lambda}^{-\mathrm{T}}, \quad \hat{\mathbf{K}}_G = \mathbf{\Lambda}^{-1} \mathbf{K}_G \mathbf{\Lambda}^{-\mathrm{T}}, \quad \hat{\mathbf{d}} = \mathbf{\Lambda} \mathbf{d}, \quad \hat{\underline{\mathbf{M}}} = \mathbf{\Lambda}^{-1} \underline{\mathbf{M}} \mathbf{\Lambda}^{-\mathrm{T}} \tag{17}$$

and the transformation matrix is computed as $\mathbf{\Lambda}_{IJ} = \mathbf{N}_I^a(\mathbf{x}_J)\mathbf{I}$, where $\mathbf{I}$ is a $3 \times 3$ identity matrix.

## 3. Numerical results and discussions

### 3.1. Numerical implementation

The reproducing kernel shape functions are computed by imposing the reproducing conditions on the kernel function values of a set of particles in the discretized solution domain. In this study, the cubic B-spline window function $\mathbf{\Phi}$, given below, is used to construct the kernel function $\mathbf{\Phi}_a(\mathbf{x} - \mathbf{x}_I)$ as

$$\mathbf{\Phi}_a(s_I) = \frac{1}{a_I} \mathbf{\Phi}\left(\frac{s_I}{a_I}\right) = \begin{cases} \frac{2}{3} - 4\left(\frac{s_I}{a_I}\right)^2 + 4\left(\frac{s_I}{a_I}\right)^3 & \frac{s_I}{a_I} \leqslant \frac{1}{2}, \\ \frac{4}{3} - 4\frac{s_I}{a_I} + 4\left(\frac{s_I}{a_I}\right)^2 - \frac{4}{3}\left(\frac{s_I}{a_I}\right)^3 & \frac{1}{2} < \frac{s_I}{a_I} \leqslant 1, \\ 0 & \frac{s_I}{a_I} > 1, \end{cases} \tag{18}$$

where $s_I = |x - x_I|$ and $a_I$ is the dilation parameter to measure the domain of influence of the particle $x_I$. In the numerical implementation of the kernel approximate, the dilation parameter $a$ is defined as $a_I = r\Delta_I$ where $r$ is a scaling factor, and $\Delta_I$ is the larger distance to $x_I$, its nearest neighbor in a one-dimensional case. In this two-dimensional analysis, the domains of influence are set as rectangular shapes, and the dilation parameters become $a_{xI}$ and $a_{yI}$ in the $(x, y)$ co-ordinate system. And the kernel function values $\mathbf{\Phi}_a(\mathbf{x} - \mathbf{x}_I)$ are computed as

$$\mathbf{\Phi}_a(\mathbf{x} - \mathbf{x}_I) = \frac{1}{a_{xI}}\mathbf{\Phi}\left(\frac{x - x_I}{a_{xI}}\right)\frac{1}{a_{yI}}\mathbf{\Phi}\left(\frac{y - y_I}{a_{yI}}\right), \tag{19}$$

where $a_{xI} = r_x\Delta_{xI}$ and $a_{yI} = r_y\Delta_{yI}$, in which the scaling factors $r_x$ and $r_y$ are adjustable to control the size of domains of influence, and $\Delta_{xI}$ and $\Delta_{yI}$ are defined as the average distances between the adjacent particles along the $x$ and $y$ directions in a regular discretization. In this study, $r_x = r_y \approx 3.5$.

In the Gaussian integration for the stiffness matrices, unless otherwise indicated, the integration order of $4 \times 4$ is used in this paper. The integration uses a 2-D regular background mesh. When the particles are uniformly distributed, the intersection points of the background meshes are coincident with the discrete particles. When the particles are randomly distributed within the domain, the same integration background mesh is used. In the following analysis of free vibration of rectangular plates, a uniform $17 \times 17$ particle distribution is adopted for all the cases considered.

### 3.2. Free vibration of plates

#### 3.2.1. Square isotropic Mindlin/Reissner plates

The effectiveness of the RKPM for vibration analysis of Mindlin/Reissner plates are demonstrated by examples of square Mindlin/Reissner plates with different boundary conditions. The geometry of the plates is as shown as in Fig. 1. The length of each edge is $a$, and two thickness-to-side ratios $t/a = 0.01$ and 0.1 are considered. The effects of shear deformation are considered and the shear correction factors are employed accordingly, so as to compare with the corresponding results from other analyses.

A non-dimensional frequency parameter is defined as

$$\Omega_{mn} = \omega_{mn}a\sqrt{\frac{\rho}{G}}, \tag{20}$$

where $\omega_{mn}$ is the frequency, $a$ is the plate side length, $\rho$ is the mass density per unit volume, $G$ is the shear modulus and $G = E/2(1 + \nu)$, $E$ Young's modulus and $\nu$ the Poisson ratio. The subscripts $m$ and $n$ are the number of half-waves in the modal shapes in the $x$ and $y$ directions, respectively.

Firstly, two fully clamped Mindlin/Reissner square plates (CCCC) with different thickness-to-edge ratios are considered. The plates are clamped at all the boundary edges. The first thirteen modes of vibration for both the plates are calculated. In this boundary condition case, the shear correction factor is taken as $k^2 = 0.8601$. Two cases of thickness-to-edge ratios are considered, i.e., $t/a = 0.1$ and 0.01. The comparison of frequency parameters

Table 1
Frequency parameters $\Omega_{mn}$ for a CCCC square Mindlin/Reissner plate with $t/a = 0.1$, $k^2 = 0.8601$, $v = 0.3$

| Mode no. | $m$ | $n$ | Rayleigh–Ritz [16] | Present (Meshfree) |
|---|---|---|---|---|
| 1 | 1 | 1 | 1.594 | 1.5582 |
| 2 | 2 | 1 | 3.039 | 3.0182 |
| 3 | 1 | 2 | 3.039 | 3.0182 |
| 4 | 2 | 2 | 4.265 | 4.1711 |
| 5 | 3 | 1 | 5.035 | 5.1218 |
| 6 | 1 | 3 | 5.078 | 5.1594 |
| 7 | 3 | 2 | — | 6.0178 |
| 8 | 2 | 3 | — | 6.0178 |
| 9 | 4 | 1 | — | 7.5169 |
| 10 | 1 | 4 | — | 7.5169 |
| 11 | 3 | 3 | — | 7.7288 |
| 12 | 4 | 2 | — | 8.3985 |
| 13 | 2 | 4 | — | 8.3985 |

Table 2
Frequency parameters $\Omega_{mn}$ for a CCCC square Mindlin/Reissner plate with $t/a = 0.01$, $k^2 = 0.8601$, $v = 0.3$

| Mode no. | $m$ | $n$ | Rayleigh–Ritz [16] | Present (Meshfree) |
|---|---|---|---|---|
| 1 | 1 | 1 | 0.1754 | 0.1743 |
| 2 | 2 | 1 | 0.3576 | 0.3576 |
| 3 | 1 | 2 | 0.3576 | 0.3576 |
| 4 | 2 | 2 | 0.5274 | 0.5240 |
| 5 | 3 | 1 | 0.6402 | 0.6465 |
| 6 | 1 | 3 | 0.6432 | 0.6505 |
| 7 | 3 | 2 | — | 0.8015 |
| 8 | 2 | 3 | — | 0.8015 |
| 9 | 4 | 1 | — | 1.0426 |
| 10 | 1 | 4 | — | 1.0426 |
| 11 | 3 | 3 | — | 1.0628 |
| 12 | 4 | 2 | — | 1.1823 |
| 13 | 2 | 4 | — | 1.1823 |

with the Rayleigh–Ritz solutions [16] for each plate is listed in Tables 1 and 2. Excellent agreement is obtained. In Fig. 2, some of the modal shapes of the CCCC plate ($t/a = 0.1$) are also presented.

Secondly, fully simply supported Mindlin/Reissner square plates with different thickness-to-edge ratios are considered. The first thirteen modes of vibration have been calculated. The frequency parameters for two cases of thickness-to-edge ratios $t/a = 0.1$ and 0.01, are listed in Tables 3 and 4. Comparison with 3-D elasticity and Mindlin closed form solutions [20] showed excellent agreement.

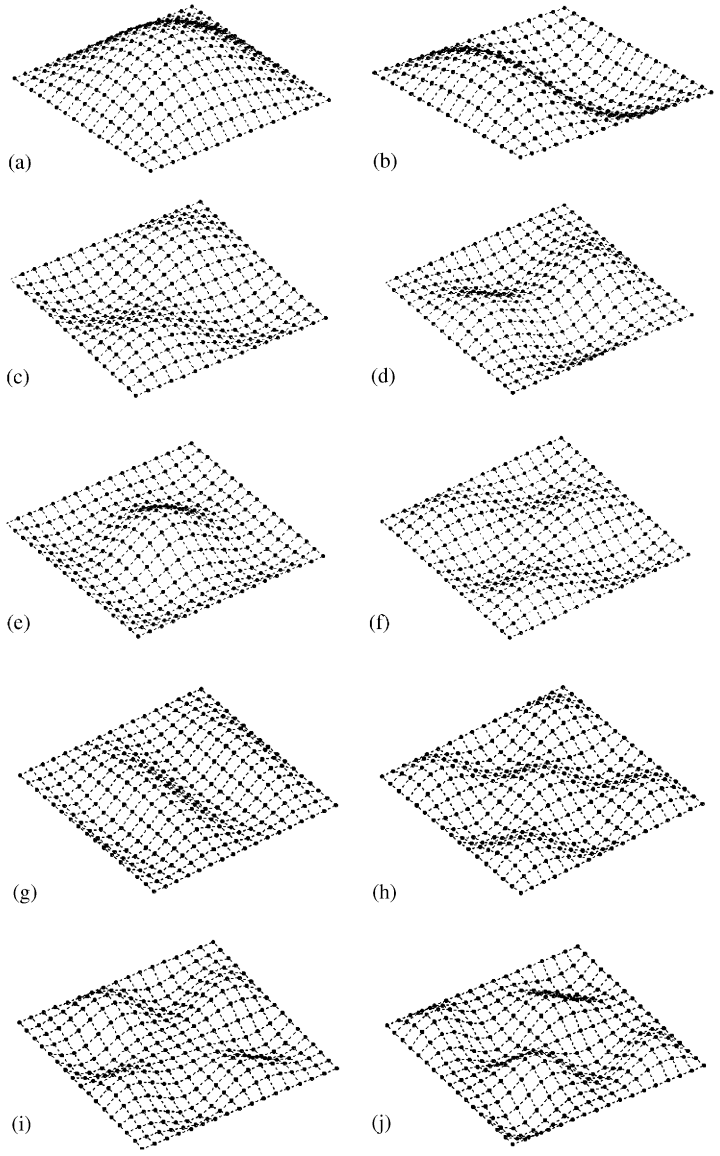


Fig. 2. The free vibration modal shapes of a CCCC square isotropic Mindlin/Reissner plate. (a) 1st Mode ($m = 1$, $n = 1$); (b) 3rd Mode ($m = 1, n = 2$); (c) 4th Mode ($m = 2, n = 2$); (d) 5th Mode ($m = 3, n = 1$); (e) 6th Mode ($m = 1, n = 3$); (f) 7th Mode ($m = 3, n = 2$); (g) 10th Mode ($m = 4, n = 1$); (h) 11th Mode ($m = 3, n = 3$); (i) 12th Mode ($m = 4, n = 2$); (j) 13th Mode ($m = 2, n = 4$).

### 3.2.2. *Circular Mindlin/Reissner plates*

In this example, the free vibration of a clamped circular plate is studied. The whole plate is modelled with almost uniformly distributed particles as shown in Fig. 3. The plate has Young's modulus $E$, thickness $t$, the Poisson ratio $v$, mass density $\rho$ and radius $R$, and the non-dimensional

Table 3
Frequency parameters $\Omega_{mn}$ for an SSSS Mindlin/Reissner plate with $t/a = 0.1$, $k^2 = 0.833$, $v = 0.3$

| Mode no. | $m$ | $n$ | 3D closed form | Mindlin closed form | Meshfree |
|---|---|---|---|---|---|
| 1 | 1 | 1 | 0.932 | 0.930 | 0.922 |
| 2 | 2 | 1 | 2.226 | 2.219 | 2.205 |
| 3 | 1 | 2 | 2.226 | 2.219 | 2.205 |
| 4 | 2 | 2 | 3.421 | 3.406 | 3.377 |
| 5 | 3 | 1 | 4.171 | 4.149 | 4.139 |
| 6 | 1 | 3 | 4.171 | 4.149 | 4.139 |
| 7 | 3 | 2 | 5.239 | 5.206 | 5.170 |
| 8 | 2 | 3 | 5.239 | 5.206 | 5.170 |
| 9 | 4 | 1 | — | 6.520 | 6.524 |
| 10 | 1 | 4 | — | 6.520 | 6.524 |
| 11 | 3 | 3 | 6.889 | 6.834 | 6.779 |
| 12 | 4 | 2 | 7.511 | 7.446 | 7.416 |
| 13 | 2 | 4 | 7.511 | 7.446 | 7.416 |

Table 4
Frequency parameters $\Omega_{mn}$ for an SSSS square Mindlin/Reissner plate with $t/a = 0.01$, $h^2 = 0.833$, $v = 0.3$

| Mode no. | $m$ | $n$ | Mindlin closed form | Present (Meshfree) |
|---|---|---|---|---|
| 1 | 1 | 1 | 0.09629 | 0.0961 |
| 2 | 2 | 1 | 0.2406 | 0.2419 |
| 3 | 1 | 2 | 0.2406 | 0.2419 |
| 4 | 2 | 2 | 0.3848 | 0.3860 |
| 5 | 3 | 1 | 0.4809 | 0.4898 |
| 6 | 1 | 3 | 0.4809 | 0.4898 |
| 7 | 3 | 2 | 0.6249 | 0.6315 |
| 8 | 2 | 3 | 0.6249 | 0.6315 |
| 9 | 4 | 1 | 0.8167 | 0.8447 |
| 10 | 1 | 4 | 0.8167 | 0.8447 |
| 11 | 3 | 3 | 0.8647 | 0.8726 |
| 12 | 4 | 2 | 0.9605 | 0.9822 |
| 13 | 2 | 4 | 0.9605 | 0.9822 |

frequency parameter is defined as

$$\lambda_f = \omega R^2 \sqrt{\rho\, t/D}, \tag{21}$$

where $D$ is the flexural rigidity defined as $D = Et^3/[12(1 - v^2)]$. The frequency parameters for plates with thickness-to-edge ratios $t/R = 0.1$ and 0.01 are presented in Tables 5 and 6. Comparisons with results of Liew et al. [28] and Hinton [20] show excellent agreement. Fig. 4 presents the lower order vibration modal shapes.

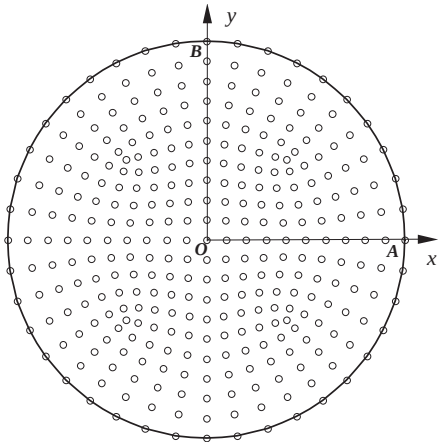


Fig. 3. Full model of the circular plate.

Table 5
Frequency parameters $\lambda_f$ $(= \omega R^2\sqrt{\rho h/\bar{D}})$ for a clamped circular Mindlin/Reissner plate with thickness to radius ratio: $t/R = 0.1$

| $n$ | $s$ | Exact [28] | Present (Meshfree) |
|---|---|---|---|
| 0 | 1 | 9.941 | 9.931 |
| | 2 | 36.479 | 36.665 |
| | 3 | 75.664 | 76.531 |
| | 4 | 123.32 | 122.46 |
| 1 | 1 | 20.232 | 20.194 |
| | 2 | 53.890 | 54.257 |
| | 3 | 97.907 | 99.207 |
| 2 | 0 | 32.406 | 32.353 |
| | 1 | 72.368 | 72.669 |
| | 2 | 120.55 | 121.94 |
| 3 | 0 | 46.178 | 45.827 |
| | 1 | 91.712 | 92.267 |
| 4 | 0 | 61.272 | 60.6595 |
| | 1 | 111.74 | 110.68 |
| 5 | 0 | 77.454 | 76.5343 |
| 6 | 0 | 94.527 | 93.285 |

Table 6
Frequency parameters $\lambda_f$ $(= \omega R^2\sqrt{\rho h/\bar{D}})$ for a clamped circular Mindlin/Reissner plate with the thickness to radius ratio: $t/R = 0.01$

| $n$ | $s$ | Finite element [20] | Present (Meshfree) |
|---|---|---|---|
| 0 | 1 | 10.2158 | 10.2661 |
| | 2 | 39.771 | 40.2905 |
| 1 | 1 | 21.26 | 21.4488 |
| | 2 | 60.82 | 62.1455 |
| 2 | 0 | 34.88 | 35.2556 |
| | 1 | 84.58 | 86.3649 |
| 3 | 0 | 51.04 | 51.6626 |
| | 1 | 111.01 | 113.594 |
| 4 | 0 | 69.6659 | 70.4145 |
| | 1 | 140.108 | 142.119 |

### 3.3. Buckling of plates

In the following examples, the non-dimensional buckling load intensity factor is defined as

$$K_b = b^2 N_{cr}/(\pi^2 D), \tag{22}$$

where $b$ is the edge length of the plate, $N_{cr}$ the critical buckling load, and $D$ the flexural rigidity.

#### 3.3.1. Simply supported rectangular plates subjected to uniaxial compression

The rectangular isotropic plate under consideration is simply supported on each edge, see Fig. 5(a). The plate is modelled with uniform particles, as well as with randomly distributed particles. When generating the random particles, the generator code controls the distances among the particles to avoid extremely closed particles so as to ensure the stiffness matrices non-singular. The particles on the edges are still uniformly built as Fig. 5(b) shows. In Fig. 5(b), the plate is discretized by $17 \times 17$ random particles, where we mentioned $17 \times 17$ because each edge has 17 uniform particles and the total number of the particles are equal to that of a uniform $17 \times 17$ discretization. Also $\Delta_{xI}$ and $\Delta_{yI}$ are the same as those in a regular discretization. Three different thickness-to-width ratios, $t/b = 0.05$, 0.1, 0.2, and five width-to-length ratios, $a/b = 0.5$, 1, 1.5, 2, 2.5 are considered. Present results are compared with those of the pb-2 Ritz method presented by Kitipornchai et al. [6] and details tabulated in Table 7. It is observed that the present predictions are very close to the pb-2 Ritz results for both cases of uniform and randomly distributed particles. Fig. 6 is a plot of the critical buckling load factor against the length-to-width ratio, $a/b$. Further, the buckling mode shapes for different length-to-width ratios are shown in Fig. 7.

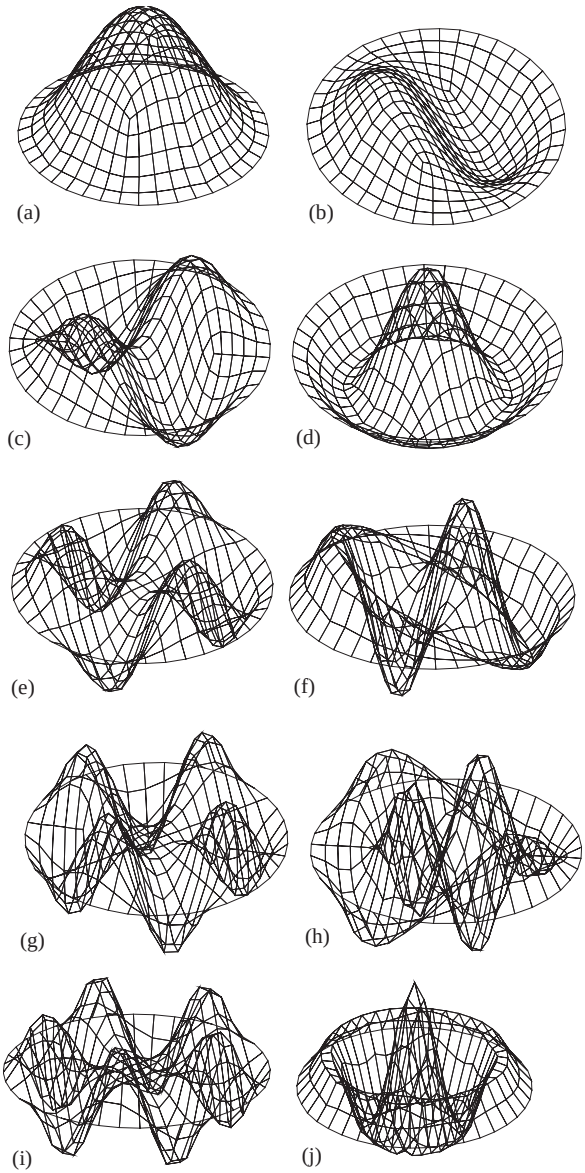


Fig. 4. Free vibration modal shapes of a clamped circular Mindlin/Reissner plate. (a) 1st Mode; (b) 2nd Mode; (c) 4th Mode; (d) 6th Mode; (e) 7th Mode; (f) 9th Mode; (g) 11th Mode; (h) 13th Mode; (i) 15th Mode; (j) 17th Mode.

### *3.3.2. Compression buckling behavior of skew plates*

This example has also been considered by Kitipornchai et al. [6] and Wang et al. [29] using the p-version Ritz function method. Skew plates, as shown in Fig. 8, with skew angle, $\alpha$, thickness-to-width ratio, $t/b$, and different combinations of edge support conditions, are examined. The plate is modelled with $17 \times 17$ distributed particles, and $4 \times 4$ integration rules is employed, see Fig. 9.

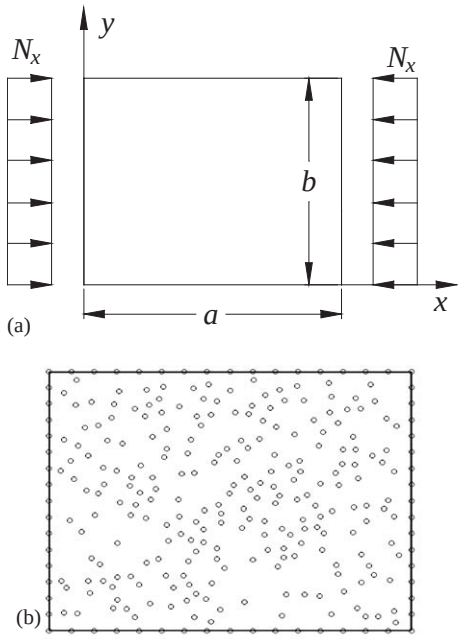


Fig. 5. Rectangular plate subjected to in-plane compression loading.

Table 7
Critical buckling load intensity factors, $K_b$, of simply-supported rectangular plates with different length-to-width ratios, $a/b$, and thickness-to-width ratios, $t/b$, subjected to uniaxial compression

| $a/b$ | $t/b$ | Present (Meshfree) | | Kitipornchai et al. [6] (pb-2 Ritz) |
|---|---|---|---|---|
| | | Regular particles | Irregular particles | |
| 0.5 | 0.05 | 6.0405 | 5.9624 | 6.0372 |
| | 0.1 | 5.3116 | 5.2084 | 5.4777 |
| | 0.2 | 3.7157 | 3.6933 | 3.9963 |
| 1 | 0.05 | 3.9293 | 3.9610 | 3.9444 |
| | 0.1 | 3.7270 | 3.6760 | 3.7865 |
| | 0.2 | 3.1471 | 3.0750 | 3.2637 |
| 1.5 | 0.05 | 4.2116 | 4.2849 | 4.2570 |
| | 0.1 | 3.8982 | 3.8761 | 4.0250 |
| | 0.2 | 3.1032 | 3.0505 | 3.3048 |
| 2 | 0.05 | 3.8657 | 4.0511 | 3.9444 |
| | 0.1 | 3.6797 | 3.6714 | 3.7865 |
| | 0.2 | 3.0783 | 3.1040 | 3.2637 |
| 2.5 | 0.05 | 3.9600 | 4.1423 | 4.0645 |
| | 0.1 | 3.7311 | 3.6985 | 3.8683 |
| | 0.2 | 3.0306 | 2.9520 | 3.2421 |

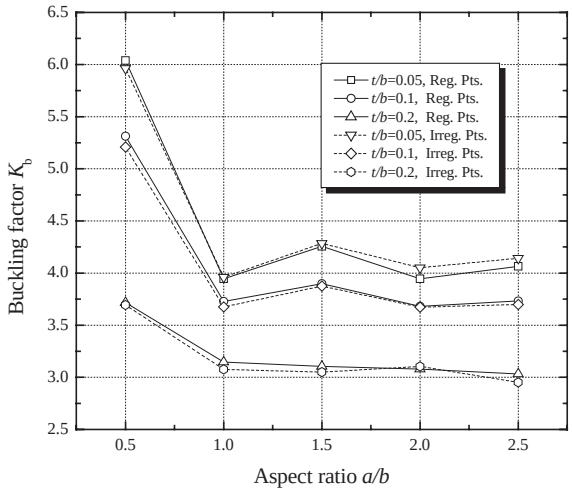


Fig. 6. Critical buckling load intensity factors, $K_b$, of simply-supported rectangular plates under uniaxial compression at various length-to-width and thickness-to-width ratios.

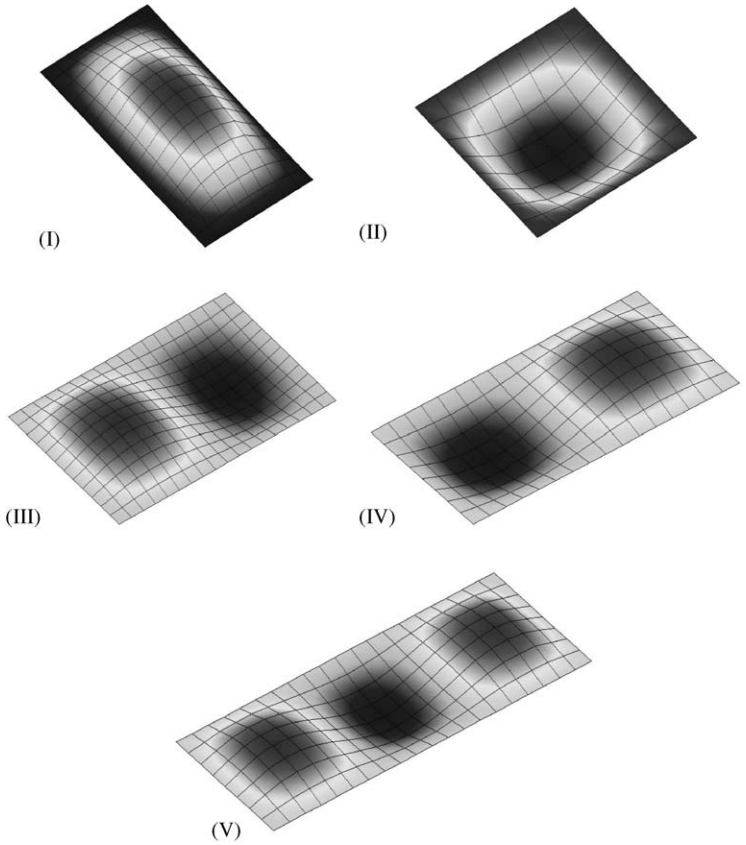


Fig. 7. Buckling mode of simply-supported rectangular plates at various length-to-width ratios, $t/b = 0.01$. (I) $a/b = 0.5$; (II) $a/b = 1$; (III) $a/b = 1.5$; (IV) $a/b = 2$; (V) $a/b = 2.5$.

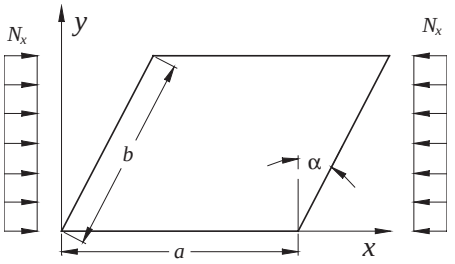


Fig. 8. Skew plate under uniaxial in-plane loading.

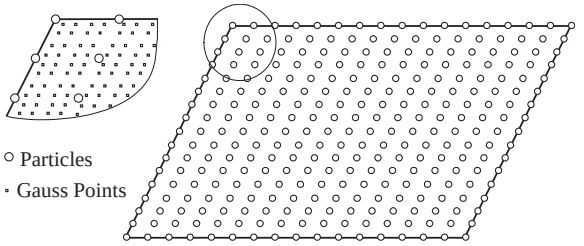


Fig. 9. Particles and integration points for the skew plate.

Numerical results for thick plates with thickness-to-width ratios, $t/b = 0.05$, 0.1, skew angles, $\alpha = 0°$, 15°, 30°, 45°, and various boundary conditions of SSSS, CCCC and FCFC, are compared with those of Kitipornchai et al. [6] and presented in Table 8. In Table 8, S, C and F denote simply supported, clamped and free boundary conditions, respectively. Based on the favorable comparisons observed in Table 8, it can be concluded that the plate buckling load intensity factors are well approximated by the meshfree method.

Figs. 10 and 11 show the variation of the buckling load intensity factor with different skew angles at $t/b = 0.05$ and 0.1, respectively. As expected, the shear-deformation effect becomes more important as the plate thickness-to-width ratio, $t/b$, increases. It is observed from these two figures that the buckling load intensity factor decreases with increasing thickness-to-width ratio, $t/b$. This decrease in the buckling load intensity factor occurs most significantly for the CCCC case. Also, the buckling load intensity factor is observed to increase with increasing skew angles, $\alpha$.

### 3.3.3. *Rectangular plate in shear*

We now consider the shear load buckling analysis of rectangular plates with simply supported boundary conditions, see Fig. 12. The plate configurations considered here have a thickness-to-width ratio of $t/b = 0.01$ and with the length-to-width ratios of $a/b = 1$, 2, 3, 4. Numerical results compared with the exact solution [30] are presented in Table 9. The local shear buckling coefficients, $K_s$, are non-dimensionalized in similar fashion to $K_b$ in Eq. (22). Fig. 13 shows the variation of the shear buckling load intensity factors with the length-to-width ratio. Fig. 14 plots the local shear buckling modes for different length-to-width aspect ratios. It is observed

Table 8
Critical buckling load factors, $K_b$, for skew plates with various boundary conditions and under uniaxial loads

| Boundary condition | $t/b$ | Skew angle | Present (Meshfree) | Kitipornchai et al. [6] (pb-2 Ritz) |
|---|---|---|---|---|
| SSSS | 0.1 | 0° | 3.7270 | 3.7870 |
| | | 15° | 4.0472 | 4.1412 |
| | | 30° | 4.8534 | 4.9324 |
| | | 45° | 7.6106 | 7.7236 |
| | 0.05 | 0° | 3.9293 | 3.9444 |
| | | 15° | 4.3260 | 4.3280 |
| | | 30° | 5.3874 | 5.4182 |
| | | 45° | 8.6926 | 8.7382 |
| CCCC | 0.1 | 0° | 8.1849 | 8.2917 |
| | | 15° | 8.7560 | 8.7741 |
| | | 30° | 10.3273 | 10.3760 |
| | | 45° | 13.2881 | 13.6909 |
| | 0.05 | 0° | 9.5418 | 9.5588 |
| | | 15° | 10.2123 | 10.2312 |
| | | 30° | 12.5225 | 12.5711 |
| | | 45° | 17.8211 | 17.9652 |
| FCFC | 0.1 | 0° | 3.5063 | 3.5077 |
| | | 15° | 3.7684 | 3.7937 |
| | | 30° | 4.7773 | 4.8043 |
| | | 45° | 6.3092 | 6.3311 |
| | 0.05 | 0° | 3.7984 | 3.8007 |
| | | 15° | 4.1310 | 4.1387 |
| | | 30° | 5.3510 | 5.3660 |
| | | 45° | 7.3658 | 7.4670 |

simultaneously from Table 9 and Fig. 13 that the critical shear load intensity factors decrease rapidly as the plate aspect ratio $a/b$ is increased from 1 to 4. Also it can be observed from Figs. 7 and 14 that the local shear buckling modes are clearly distinct from the axial compression buckling modes.

## 4. Conclusions

A meshfree method based upon the reproducing kernel particle approximation, for the free vibration and buckling analyses of thick plates, has been described. The approach discretizes the domain in terms of particles and does not rely on the connectivity of elements as in the finite element method. It can alleviate the difficulties of meshing or remeshing. However, a background mesh is still used for Gauss integration. During numerical implementations, a generic particle is

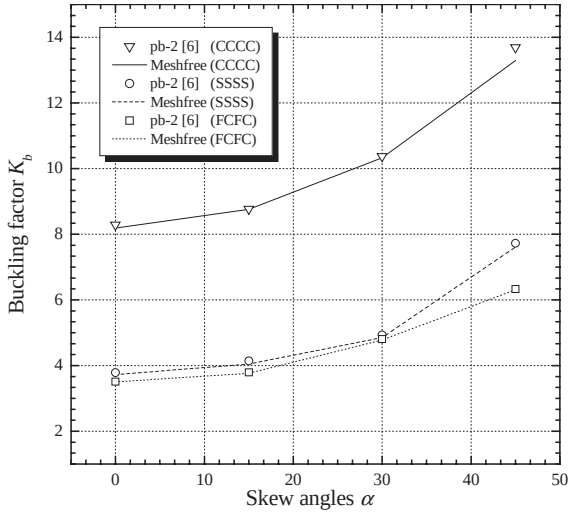


Fig. 10. Variation of critical buckling load factor, $K_b$, with skew angle, $\alpha$, ($a/b = 1$ and $t/b = 0.1$).

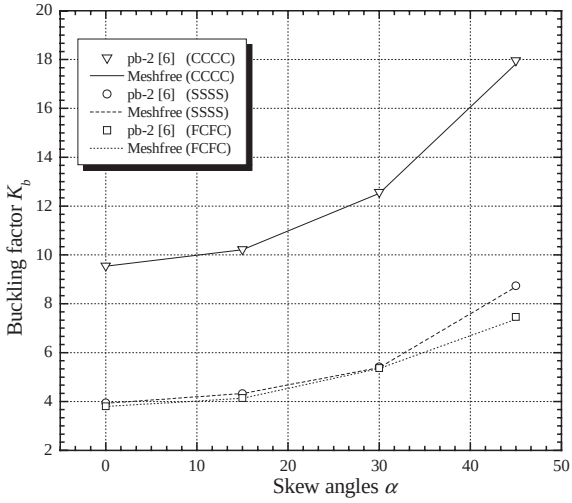


Fig. 11. Variation of critical buckling load, $K_b$, with skew angle, $\alpha$, ($a/b = 1$ and $t/b = 0.05$).

influenced by others within its domain of influence, and usually the numbers should be large enough to avoid singularity of the stiffness matrices. This causes the computing cost to be higher than that of the FEM.

In this paper, the transverse shear effect is accounted for using the first order shear-deformation theory of the Mindlin/Reissner type. As cubic and quadratic kernel functions were adopted in the computation, no shear and membrane locking was observed. Transformation algorithms have been used to impose the essential boundary conditions. Consequently, the essential boundary conditions are imposed in a manner reminiscent of the FEM method. Numerical free vibration

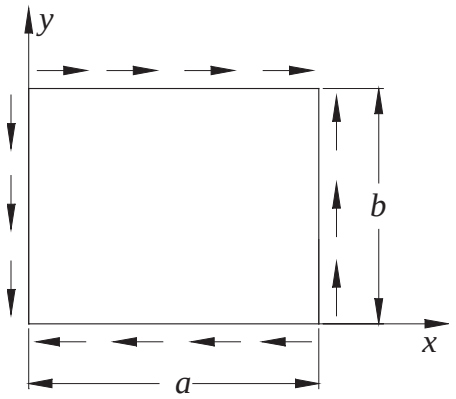


Fig. 12. A rectangular plate subjected to pure shear.

Table 9
Shear buckling factors, $K_s$, of simply supported rectangular plates at various length-to-width ratios. The thickness-to-width ratio is taken to be $t/b = 0.01$

| $a/b$ | Present (Meshfree) | Azhari et al. [30] (Exact) |
|---|---|---|
| 1 | 9.3962 | 9.34 |
| 2 | 6.3741 | 6.34 |
| 3 | 5.7232 | 5.784 |
| 4 | 5.4367 | 5.59 |

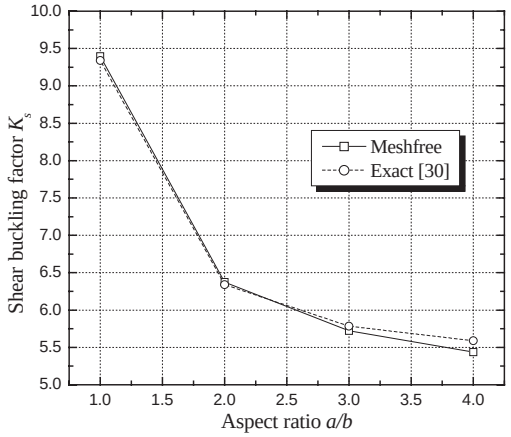


Fig. 13. Variation of critical local shear buckling load intensity factor, $K_s$, with length-to-width ratio for simply-supported rectangular plates, $t/b = 0.01$.

solutions for plates with different geometrical shapes and boundary conditions, and buckling solutions with various aspect ratios, skew angles and boundary conditions subjected to uniaxial compression and pure shear loading show that the present approach is an accurate and effective tool for this class of problems.

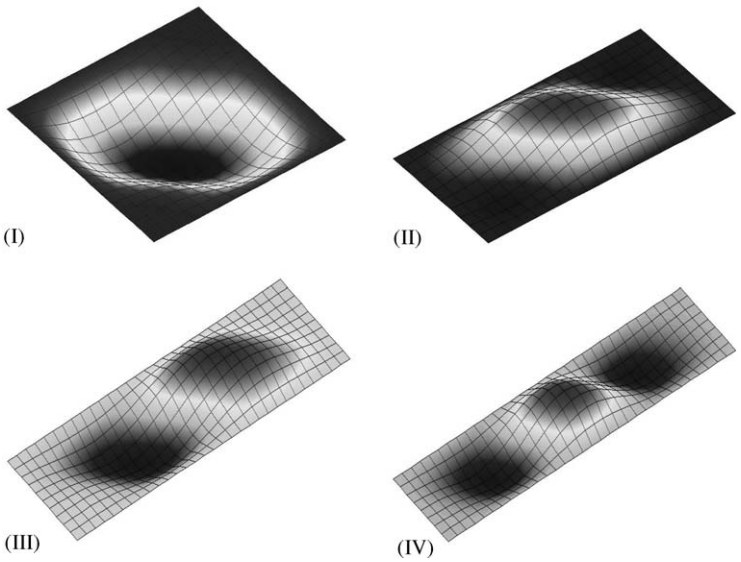


Fig. 14. Shear buckling modes of simply-supported rectangular plates at various length-to-width ratios, $t/b = 0.01$.

## References

[1] Lord Rayleigh. *Theory of Sound*, Vol. 1, 1887, Macmillan, London, reprinted in 1945, Dover, New York.
[2] K.M. Liew, Y. Xiang, S. Kitipornchai, Research on thick plate vibration: a literature survey, *Journal of Sound and Vibration* 180 (1) (1995) 163–176.
[3] A.K. Noor, Free vibrations of multilayered composite plates, *American Institute of Aeronautics and Astronautics Journal* 11 (7) (1973) 1038–1039.
[4] J.N. Reddy, A review of refined theories of laminated composite plates, *The Shock and Vibration Digest* 22 (7) (1990) 3–17.
[5] A. Tessler, E. Saether, T. Tsui, Vibration of thick laminated composite plates, *Journal of Sound and Vibration* 179 (3) (1995) 475–498.
[6] S. Kitipornchai, Y. Xiang, C.M. Wang, K.M. Liew, Buckling of thick skew plates, *International Journal for Numerical Methods in Engineering* 36 (1993) 1299–1310.
[7] Y. Xiang, G.H. Su, Buckling of rectangular plates with mixed edge supports, *Structural Engineering and Mechanics* 14 (4) (2002) 401–416.
[8] Y. Xiang, Buckling of triangular plates with elastic edge constraints, *Acta Mechanica* 156 (1–2) (2002) 63–77.
[9] W. Han, S.M. Dickinson, Free vibration of symmetrically laminated skew plates, *Journal of Sound and Vibration* 208 (3) (1997) 367–390.
[10] J. Yuan, S.M. Dickinson, On the vibration of annular, circular and sectorial plates with cut-outs or on partial supports, *Computers and Structures* 58 (6) (1996) 1261–1264.
[11] P.A.A. Laura, D.R. Avalos, H.A. Larrondo, R.E. Rossi, Numerical experiments on the Rayleigh–Ritz method when applied to doubly connected plates in the case of free edge holes, *Ocean Engineering* 25 (7) (1998) 585–589.
[12] P.A.A. Laura, R.H. Gutierrez, H.C. Sanzi, G. Elvira, Buckling of circular, solid and annular plates with an intermediate circular support, *Ocean Engineering* 27 (7) (2000) 749–755.
[13] D. Zhou, Y.K. Cheung, F.T.K. Au, S.H. Lo, Three-dimensional vibration analysis of thick rectangular plates using Chebyshev polynomial and Ritz method, *International Journal of Solids and Structures* 39 (26) (2002) 6339–6353.

[14] D. Zhou, Vibrations of point-supported rectangular plates with variable thickness using a set of static tapered beam functions, *International Journal of Mechanical Sciences* 44 (1) (2002) 149–164.
[15] Y. Narita, K. Fukushi, X.L. Zhao, Vibration analysis of shear-deformable circular and elliptical laminated composite plates, *JSME International Journal Series C—Mechanical Systems Machine Elements and Manufacturing* 45 (1) (2002) 113–120.
[16] D.J. Dawe, O.L. Roufaeil, Rayleigh-Ritz vibration analysis of Mindlin plates, *Journal of Sound and Vibration* 69 (3) (1980) 345–359.
[17] H. Zeng, C.W. Bert, A differential quadrature analysis of vibration for rectangular stiffened plates, *Journal of Sound and Vibration* 241 (2) (2001) 247–252.
[18] C.W. Bert, M. Malik, The differential quadrature method for irregular domains and application to plate vibration, *International Journal of Mechanical Sciences* 38 (6) (1996) 589–606.
[19] D.J. Dawe, S. Wang, Spline finite strip analysis of the buckling and vibration of rectangular composite laminated plates, *International Journal of Mechanical Sciences* 37 (6) (1995) 645–667.
[20] E. Hinton, *Numerical Methods and Software for Dynamic Analysis of Plates and Shells*, Pineridge Press, Swansea, U.K, 1988.
[21] J.N. Reddy, A.A. Khdeir, Buckling and vibration of laminated composite plates using various plate theories, *American Institute of Aeronautics and Astronautics Journal* 27 (12) (1989) 1808–1817.
[22] A.W. Leissa, A review of laminated composite plate buckling, *Applied Mechanics Reviews* 40 (5) (1987) 575–591.
[23] A.W. Leissa, Buckling and postbuckling theory for laminated composite plates, in: G.J. Turvey, I.H. Marshall (Eds.), *Buckling and Postbuckling of Composite Plates*, Chapman & Hall, London, UK, 1995, pp. 1–29.
[24] R.K. Kapania, S. Raciti, Recent advances in analysis of laminated beams and plates, Part I: Shear effects and buckling, *American Institute of Aeronautics and Astronautics Journal* 27 (7) (1989) 923–934.
[25] K.M. Liew, Y. Xiang, S. Kitipornmchai, J.L. Meek, Formulation of Mindlin-Engesser model for stiffened plate vibration, *Computer Methods in Applied Mechanics and Engineering* 120 (4) (1995) 339–353.
[26] J.S. Chen, C. Pan, C.T. Wu, W.K. Liu, Reproducing kernel particle methods for large deformation analysis of non-linear structures, *Computer Methods in Applied Mechanics and Engineering* 139 (2) (1996) 195–227.
[27] J.S. Chen, H.P. Wang, New boundary condition treatments in meshfree computation of contact problems, *Computer Methods in Applied Mechanics and Engineering* 187 (3) (2000) 441–468.
[28] K.M. Liew, C.M. Wang, Y. Xiang, S. Kitipornchai, *Vibration of Mindlin Plates*, Elsevier, Amsterdam, 1998.
[29] C.M. Wang, S. Kitipornchai, Y. Xiang, K.M. Liew, Stability of skew Mindlin plates under isotropic in-plane pressure, *Journal of Engineering Mechanics, American Society of Civil Engineers* 119 (3) (1993) 393–401.
[30] M. Azhari, S. Hoshdar, M.A. Bradford, On the use of bubble functions in the local buckling analysis of plate structures by the spline finite strip method, *International Journal for Numerical Methods in Engineering* 48 (4) (2000) 583–593.